

Tilt-based Aberration Estimation in Transmission Electron Microscopy*

Jilles S. van Hulst^{a,*}, Erik M. Franken^b, Bart J. Janssen^b, W.P.M.H. (Maurice) Heemels^a, Duarte J. Antunes^a

^a*Department of Mechanical Engineering, Control Systems Technology Section, Eindhoven University of Technology, Eindhoven, PO Box 513, 5600MB, the Netherlands*

^b*Thermo Fisher Scientific, Eindhoven, de Schakel 2, 5651GH, the Netherlands*

Abstract

Transmission electron microscopes (TEMs) enable atomic-scale imaging but suffer from aberrations caused by lens imperfections and environmental conditions, reducing image quality. These aberrations can be compensated by adjusting electromagnetic lenses, but this requires accurate estimates of the aberration coefficients, which can drift over time. This paper introduces a method for the estimation of aberrations in TEM by leveraging the relationship between an induced electron beam tilt and the resulting image shift. The method uses a Kalman filter (KF) to estimate the aberration coefficients from a sequence of image shifts, while accounting for the drift of the aberrations over time. The applied tilt sequence is optimized by minimizing the trace of the predicted error covariance in the KF, which corresponds to the A-optimality criterion in experimental design. We show that this optimization can be performed offline, as the cost criterion is independent of the actual measurements. The resulting non-convex optimization problem is solved using a gradient-based, receding-horizon approach with multi-starts. Additionally, we develop an approach to estimate specimen-dependent noise properties using expectation maximization (EM), which are then used to tailor the tilt pattern optimization to the specific specimen being imaged. The proposed method is validated on a real TEM set-up with several optimized tilt patterns. The results show that optimized patterns significantly outperform naive approaches and that the aberration and drift model accurately captures the underlying physical phenomena. In total, the alignment time is reduced from typically several minutes to less than a minute compared to the state-of-the-art.

Keywords: Electron Microscopy, Transmission Electron Microscopy, Aberration Estimation, Sensor Scheduling, Receding-Horizon Optimization, Kalman Filtering, Experiment Design.

1. Introduction

Transmission electron microscopy (TEM) has enabled and continues to enable scientific progress across numerous fields, including materials science, semiconductors, and life sciences. A notable example of its impact is in the development of the COVID-19 vaccine, where TEM played a critical role by enabling the visualization of the virus' spike protein [1]. What makes the TEM so powerful is its ability to produce images at the atomic scale. This capability stems from the use of electrons, which have significantly shorter wavelengths than visible light. Since resolution is inversely proportional to wavelength, the shorter the wavelength, the higher the attainable resolution.

TEM images are created by directing a beam of electrons onto a specimen and recording the electrons after they have interacted with it. However, accurately guiding the electrons is a non-trivial task. The electron beam is shaped and focused by electromagnetic lenses, which inherently suffer from high sensitivity to environmental conditions and manufacturing inconsistencies. The resulting imperfections in the electron beam

are known as aberrations. Under the presence of aberrations, the resulting TEM images suffer from reduced contrast, loss of resolution, and blurring.

Fortunately, the aberrations can be compensated by adjusting the electron optical components such as electromagnetic lenses, deflectors, and stigmators. However, this compensation is not straightforward, as the aberrations cannot be measured directly. Additionally, the aberrations drift over time due to thermal effects, mechanical vibrations, and electromagnetic field fluctuations. This limits both image quality and TEM throughput. As a result, fast and accurate estimates of the aberration values are highly desirable.

This paper introduces a method for aberration estimation in TEM, aimed at addressing image degradation and limited throughput. The approach leverages a principle from optics: tilting the electron beam in the presence of aberrations causes an apparent image shift in the x, y -plane [2], revealing information about the aberrations. While the principle of using tilt-induced image shifts to estimate aberrations has been known for decades [3, 4], previous implementations have faced significant limitations including lengthy image processing times that restrict the number of tilts. This in turn makes differentiating between specimen drift and aberration effects difficult, leading to poor estimation accuracy. Additionally, these approaches often do not model specimen drift explicitly [5].

Our approach overcomes these limitations through two key

*This work is part of the research project entitled *Learning in Motion*, a collaboration between the Eindhoven University of Technology and several industry partners. This project is co-financed by Holland High Tech, top sector High-Tech Systems and Materials, with a PPP innovation subsidy for public-private partnerships for research and development.

^aCorresponding author. Email address: j.s.v.hulst@tue.nl

innovations. First, fast GPU-based image shift tracking algorithms enable rapid processing of tilt-induced image shifts [6], which are used to estimate aberrations in a Kalman filtering framework that naturally fits the physical model and includes aberration drifting. Crucially, the speed and accuracy of these estimates depends on the choice of beam tilt sequence, which motivates the core question addressed in this research and the second key innovation: *what sequence of tilts results in the fastest and most accurate aberration estimates?*

In this paper, we formulate the tilt sequence selection as a sensor scheduling problem and propose a tailor-made solution for TEM aberration estimation. Aberrations are estimated using standard Kalman filtering, and the tilt sequence is optimized by minimizing the trace of the predicted covariance. The optimization uses gradients from multiple starting points with receding-horizon optimization. The main contributions are:

- A formulation of the tilt-based aberration estimation problem as a sensor scheduling problem, extended to include specimen drift.
- Efficient, receding-horizon gradient-based sensor scheduling optimization based on the trace of the predicted covariance matrix in the Kalman filter.
- Estimation of specimen-dependent properties using expectation maximization (EM) to tailor the optimization and estimation.
- Experimental validation of optimized patterns on a real TEM set-up.

In related work, classical aberration estimation in TEM relies on methods such as the Zemlin tableau and diffractogram analysis [7], in which many images and diffraction patterns are acquired at different defocus values. While effective, these approaches are time-consuming, do not work for every sample type, and do not account for specimen drift.

On the other hand, foundational works in sensor scheduling have developed optimization frameworks for systems where measurement acquisition can be designed to improve estimation performance [8, 9]. These ideas have been adapted to the context of Kalman filtering for linear discrete-time systems [10]. Several works address continuous scheduling parameters [11, 12] and receding-horizon optimization [13]. However, these approaches are generally not tailored to TEM aberration estimation, which includes the freedom to select the scheduling parameter at every time step and the non-convex but differentiable measurement model. This paper proposes a custom optimization method addressing these challenges, introduces EM to estimate variations in system properties, and validates the approach on real hardware.

The rest of this paper is organized as follows. Section 2 formulates the aberration estimation problem. Section 3 details the methods including the tilt-induced aberration model and tilt pattern optimization. Section 4 presents results on a real TEM set-up. Section 5 concludes the paper.

2. Problem Formulation

Transmission electron microscopy (TEM) forms high-resolution images by transmitting electrons (accelerated to 100-300 keV) through a specimen. The transmission imprints information onto the electron wave by altering its phase. This imprint is enlarged by electromagnetic lenses, which project the electron wave onto a detector. The lenses are inherently prone to imperfect focusing due to geometric and electromagnetic field characteristics and finite manufacturing precision. Additionally, environmental conditions such as temperature fluctuations and mechanical vibrations affect lens performance. These imperfections manifest as aberrations, altering the electron wavefront and reducing image resolution. Aberrations are characterized by the contrast transfer function (CTF), which describes how the electron wavefront evolves through the microscope [14]. The CTF is defined as

$$\text{CTF}(g) = E(g) \exp[-i\chi(g)], \quad (1)$$

where $g \in \mathbb{C}$ is the spatial frequency, $E(g)$ is the envelope function, and $\chi(g)$ is the wave aberration function. The variables are typically defined as complex numbers to represent 2D spatial coordinates. The envelope function $E(g)$ models coherence effects causing damping across frequencies and is assumed constant. For optimal contrast, $\exp[-i\chi(g)] \approx 1$ over a broad range of frequencies g . The wave aberration function $\chi(g)$ describes the phase shift of the electron wavefront and can be represented as

$$\chi(g) = \sum_{m,n, m-n=2p} \chi_{mn}(g), \quad (2)$$

where $m > 0$ and $p, n \geq 0$ are integers such that $m - n = 2p$. Each term $\chi_{mn}(g)$ is a polynomial of degree m in g :

$$\chi_{mn}(g) = \frac{2\pi}{\lambda} \frac{|c_{mn}|}{m} (\lambda g)^m \cos[n \arg(g) - n \arg(c_{mn})], \quad (3)$$

where λ is the electron beam wavelength, $c_{mn} \in \mathbb{C}$ denotes the aberration coefficient with order m and foldness n , and \arg denotes the phase angle of a complex number. The influence of each term can be visualized using phase plates, see Figure 1. For a comprehensive overview of aberration types and naming conventions across different notations, we refer to Barthel [14, Chapter 2.2].

By adjusting the aberration coefficients c_{mn} appropriately, we can control the phase shift and thus the CTF. The coefficients can be adjusted by changing the settings of electron optical components including electromagnetic lenses. However, the coefficients are not directly measurable and must be estimated, which motivates the need for quick and accurate estimation methods.

2.1. Tilt-induced Aberration Model

A key physical insight that can be used to estimate the aberrations is that deliberately tilting the electron beam interacts with the aberrations of the microscope. This interaction modifies the effective aberrations, which in turn leads to measurable changes in the image, such as an apparent shifting of the image [2]. We

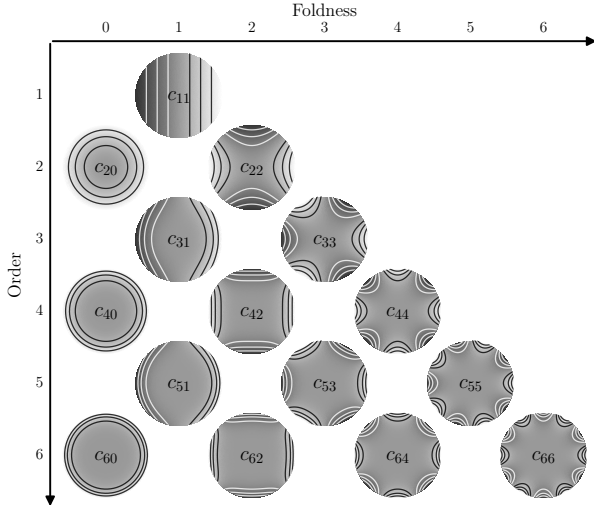


Figure 1: Phase plates of the single wave aberrations in TEM. The columns and rows correspond to the foldness and order of the aberration, respectively. Each phase plate displays the phase shift of the wavefront as a function of the spatial frequency $g \in \mathbb{C}$ in gray scale. Contour lines are plotted in white for positive phase shifts and in black for negative phase shifts. This figure has been adapted from Barthel [14, Chapter 2].

can express the effective aberrations as a function of the baseline aberrations and the electron beam tilt through

$$c'_{(\alpha+\gamma)(\alpha-\gamma)} = \rho(\alpha, \gamma) \times (\alpha + \gamma) \sum_{\beta=\alpha}^M \sum_{\delta=\gamma}^{\zeta(M, \beta)} \left[\binom{\beta}{\alpha} \binom{\delta}{\gamma} (t^*)^{\beta-\alpha} t^{\delta-\gamma} \right. \\ \left. \times \frac{c_{(\beta+\delta)(\beta-\delta)}}{\beta + \delta} + \binom{\beta}{\gamma} \binom{\delta}{\alpha} (t^*)^{\delta-\alpha} t^{\beta-\gamma} \frac{c^*_{(\beta+\delta)(\beta-\delta)}}{\beta + \delta} \right], \quad (4)$$

where $c_{mn} \in \mathbb{C}$ denotes the baseline aberration with order m and multiplicity n , $c'_{mn} \in \mathbb{C}$ denotes the effective aberration (following the tilt), and $t \in \mathbb{C}$ denotes the electron beam tilt, where t^* denotes the complex conjugate of t . M is the maximum aberration order considered. The indices $\alpha, \beta, \gamma, \delta$ are summation indices and the function $\zeta(M, \beta) = \min(\beta, M - \beta)$ limits the maximum multiplicity. The scaling factor $\rho(\alpha, \gamma)$ equals $\frac{1}{2}$ if $\alpha = \gamma$ and 1 otherwise. Note that the effective aberrations are linear in the baseline aberrations but generally nonlinear in the tilts.

Importantly, the tilt-induced image shifts c'_{11} can be quantified from a sequence of TEM images using techniques such as cross-correlations between pairs of images. Estimating the shifts from a sequence of images is called tracking and works by constructing a so-called template image, using, for example, one or more of the earlier acquired images, see e.g. van Horssen et al. [6], Bolme et al. [15]. These approaches typically need a number of near-identical images to ensure the template is initialized correctly. In our use case this can be achieved in practice by starting with relatively small initial tilts, which ensures small image changes.

Observe that the tracked image shifts c'_{11} can be linearly related to the baseline aberration coefficients by rewriting (4). In short-hand notation, we write

$$c' = \Psi(\theta)c \quad (5)$$

with $c' = (\text{Re}[c'_{11}], \text{Im}[c'_{11}])^\top \in \mathbb{R}^2$, $c \in \mathbb{R}^l$, $\Psi(\theta) \in \mathbb{R}^{2 \times l}$, and $\theta := (\text{Re}[t], \text{Im}[t])^\top \in \mathbb{R}^2$ the applied tilt. Here l is the number of aberration coefficients considered. For $M = 2$, we have $l = 5$ and obtain

$$\begin{pmatrix} \text{Re}[c'_{11}] \\ \text{Im}[c'_{11}] \end{pmatrix} = \underbrace{\begin{pmatrix} 1 & 0 & \text{Re}[t] & \text{Re}[t] & \text{Im}[t] \\ 0 & 1 & \text{Im}[t] & -\text{Im}[t] & \text{Re}[t] \end{pmatrix}}_{\Psi(\theta)} \underbrace{\begin{pmatrix} \text{Re}[c_{11}] \\ \text{Im}[c_{11}] \\ c_{20} \\ \text{Re}[c_{22}] \\ \text{Im}[c_{22}] \end{pmatrix}}_c. \quad (6)$$

From the equation, it is clear how applied tilts θ reveal the underlying aberration coefficients c through measurable shifts c' . Note that the estimation problem is complicated by the fact that the aberration drift over time due to changing environmental conditions. Additionally, the particular tilt sequence has a significant impact on estimation speed and accuracy, motivating the search for optimal tilt sequences.

3. Methods

This section presents the methodology for aberration estimation and tilt sequence optimization in TEM. The tilt-induced shift equations with an aberration drifting model admit a linear Kalman filter (KF) formulation, which allows us to estimate the aberrations in a principled way. We then detail the tilt sequence optimization method, which is the main contribution, and develop an approach to estimate specimen-dependent measurement noise covariance using expectation maximization.

3.1. Dynamic Tilt-Aberration Model

The tilt-induced shift equations (6) can be used to predict the image shift in the presence of tilts and aberrations. However, the aberrations drift due to changing environmental conditions. For this reason, we introduce a dynamic model to improve estimation accuracy by relating aberrations to a sequence of measurements. This model includes two key physical effects.

First, the specimen may move with respect to the electron beam, a phenomenon known as specimen drift. This specimen drift is indistinguishable from changes in the image displacement aberration c_{11} . We model the drift by treating c_{11} as a time-varying state using a polynomial in time of order $b \in \mathbb{N}$. Since $c_{11} \in \mathbb{C}$ is a complex number representing drift in two dimensions, the polynomial requires b complex states (or equivalently $2b$ real states). Throughout the rest of this paper, we use subscript $k \in \mathbb{N}$ to denote the discrete time index.

Second, the camera axis can in some cases be misaligned with respect to the tilt axis, resulting in relative rotation of tilt and shift coordinates. This is modeled by a state $\phi \in \mathbb{R}$ representing the rotational misalignment. We obtain a linear state-space form

$$x_{k+1} = Ax_k + \xi_k \quad (7)$$

$$y_k = C(\theta_k)x_k + \varepsilon_k \quad (8)$$

with $x_k \in \mathbb{R}^d$ the state and $y_k = c'_k \in \mathbb{R}^2$ the measurements, where $d = l + 1 + 2b$ and l is the number of aberrations considered. The states are normalized to typical values, as aberrations and drift terms differ in magnitude by several orders.

This normalization ensures that the filter remains numerically well-conditioned and that the optimization criteria (used in Section 3.3) are not dominated by large-magnitude states. The process noise is $\xi_k \sim \mathcal{N}(0, \Sigma_\xi)$ and the measurement noise is $\varepsilon_k \sim \mathcal{N}(0, \Sigma_\varepsilon)$. For $b = 2$, which results in a second-order polynomial model for specimen drift, we obtain

$$x_k = \begin{pmatrix} c_k \\ \phi_k \\ \hline \text{Re}[v_k] \\ \text{Re}[a_k] \\ \text{Im}[v_k] \\ \text{Im}[a_k] \end{pmatrix}, \quad A = \begin{pmatrix} & \begin{array}{cccc} \tau & \frac{1}{2}\tau^2 & 0 & 0 \\ 0 & 0 & \tau & \frac{1}{2}\tau^2 \\ 0 & 0 & 0 & 0 \\ & \vdots \\ 0 & 0 & 0 & 0 \end{array} \\ \hline & \begin{array}{cccc} 1 & \tau & 0 & 0 \\ 0 & 1 & 0 & 0 \\ 0 & 0 & 1 & \tau \\ 0 & 0 & 0 & 1 \end{array} \\ 0 & \end{pmatrix}, \quad (9)$$

and

$$C(\theta_k) = \begin{pmatrix} \Psi(\theta_k) & -\text{Im}[t_k] \\ \text{Re}[t_k] & \text{Re}[t_k] \end{pmatrix}, \quad (10)$$

where $v_k \in \mathbb{C}$ and $a_k \in \mathbb{C}$ are the drift velocity and acceleration at time index k , with $\text{Re}[v_k]$ and $\text{Im}[v_k]$ representing the velocity components in the x and y directions, respectively, and similarly for $\text{Re}[a_k]$ and $\text{Im}[a_k]$. τ denotes the sampling time. Essentially, the aberrations c (elements of x_k) remain constant (in the absence of process noise ξ_k), except for the shift aberrations $\text{Re}[c_{11}]$ and $\text{Im}[c_{11}]$, which are modeled as second-order polynomials in time. Note that the model can be easily extended to include polynomial drifting up to arbitrary orders of other aberrations, which would come at the cost of a more complex estimation problem. We assume the normalized initial state $x_0 \sim \mathcal{N}(0, I_d)$.

3.2. Kalman filtering for Tilt-based Aberration Estimation

To estimate the state x_k using the model (7), (8) based on a sequence of measurements y_0, \dots, y_k , we employ the Kalman Filter. The variable $\tilde{x}_{k|l}$ denotes the estimate of state x_k given measurements up to time l , i.e., $\tilde{x}_{k|l} := E[x_k | y_0, \theta_0, \dots, y_l, \theta_l]$. Similarly, $P_{k|l}$ is the estimation error covariance, $E[(x_k - \tilde{x}_{k|l})(x_k - \tilde{x}_{k|l})^T | y_0, \theta_0, \dots, y_l, \theta_l]$. The filter is initialized with $\tilde{x}_{0|0} = 0$ and $P_{0|0} = I_d$. The standard KF recursively computes estimates through update and prediction steps (see Kalman [16] for details).

The estimation could alternatively be approached using batch Linear Least Squares (LLS). For linear Gaussian systems, the KF and LLS yield equivalent estimates when the same prior knowledge is incorporated (i.e., in LLS through regularization and weighting). However, we opt for the KF framework because it naturally models aberration drift through state derivatives and process noise ξ_k , and intuitively incorporates prior beliefs via $\tilde{x}_{0|0}$, $P_{0|0}$, Σ_ε , and Σ_ξ . While these aspects can also be addressed in LLS, the Bayesian recursive nature of the KF handles them more naturally.

A key result is that the estimation error covariance P evolves independently of actual measurements [16, 9], enabling offline optimization. If A is invertible, we can batch all measurements and use N -step predicted covariances:

$$P_{N-1|N-1} = A^{(N-1)} P_{0|0} (A^\top)^{(N-1)} + \sum_{i=0}^{N-2} A^i \Sigma_\xi (A^\top)^i, \quad (11)$$

$$P_{N-1|N-1} = P_{N-1|N-1} - P_{N-1|N-1} \bar{C}^\top(\Theta_N) \Sigma^{-1}(\Theta_N) \times \bar{C}(\Theta_N) P_{N-1|N-1}, \quad (12)$$

with

$$\bar{C}(\Theta_N) = \begin{bmatrix} C(\theta_0) A^{-(N-1)} \\ C(\theta_1) A^{-(N-2)} \\ \vdots \\ C(\theta_{N-1}) \end{bmatrix}, \quad (13)$$

and

$$\Sigma(\Theta_N) = \bar{C}(\Theta_N) P_{N-1|N-1} \bar{C}^\top(\Theta_N) + I_N \otimes \Sigma_\varepsilon, \quad (14)$$

where \otimes denotes the Kronecker product, and $\Theta_N := \{\theta_i\}_{i=0}^{N-1}$ is the full tilt sequence.

Given (11)–(14), we can compare tilt sequences in terms of their impact on estimation error covariance, which is a measure of uncertainty on the aberration values. The ability to predict the estimation error covariance enables the design of sequences that minimize this uncertainty.

3.3. Optimization of Tilt Sequences

Sensor scheduling involves actively deciding sensor configurations over time to optimize an objective, typically related to estimation performance. By choosing the electron beam tilt θ_k , we change the matrix $C(\theta_k)$ in (8). The goal is to determine the N -step tilt sequence Θ_N that minimizes aberration estimation uncertainty using the predicted posterior covariance. We assess tilt pattern performance by taking a weighted trace of the predicted error covariance:

$$\begin{aligned} \min_{\Theta_N} & \text{tr}(WP_{N-1|N-1}), \\ \text{s.t.} & (11), (12), (13), (14), \\ & \|\theta_k\|_2 \leq \tilde{\theta}_k, \quad k \in \{0, 1, \dots, N-1\}, \end{aligned} \quad (15)$$

where the tilt magnitude constraint will be discussed later. By taking the covariance trace as the cost, we essentially minimize the sum of variances of each of the aberration estimates (for $W = I_d$), known as A-optimality [9]. Other common optimality criteria in experiment design include D-optimality (minimizing the determinant) and E-optimality (minimizing the largest eigenvalue), which can be interpreted as minimizing the volume of the uncertainty ellipsoid and minimizing the worst-case variance, respectively. We choose A-optimality as it provides an appropriate overall uncertainty measure and is computationally convenient, though the results extend to other criteria. In batch experiment design using LLS, criteria are frequently derived from the Fisher Information Matrix (FIM), which is the inverse of the covariance matrix. In the KF framework, working directly with the posterior covariance is a natural approach.

The matrix $W \in \mathbb{R}^{d \times d}$ is a positive semi-definite weighting matrix ($W \succeq 0$) that can be used to prioritize estimation accuracy of certain aberrations over others. This weighting is applied *after* state normalization, ensuring users express preferences among comparable state values.

We constrain the tilt magnitude to be less than a user-defined value $\tilde{\theta}_k$, which varies with time index k . This allows us to address image tracker template initialization by limiting tilts at the beginning and increasing them as tracker accuracy improves. Additionally, the tilt magnitude must be upper-bounded since (4)

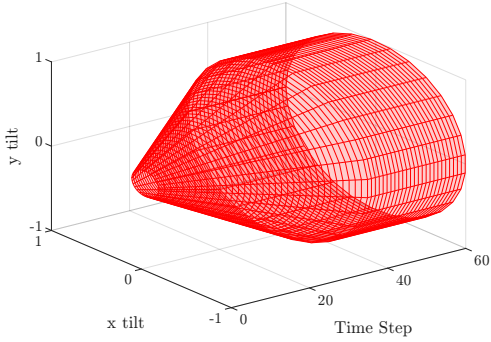


Figure 2: Example of a user-defined tilt constraint $\tilde{\theta}_k$ as a function of time k . The red lines indicate the boundaries of the feasible set. Note that the tilt values are normalized.

is only valid for small tilts. Figure 2 shows an example of the tilt magnitude constraint as a function of time.

Several aspects make this sensor scheduling problem distinct from standard sensor scheduling problems:

- 1) The sensor scheduling parameter is a *continuous*, two-dimensional vector that can be selected at *every timestep*;
- 2) The cost function $\text{tr}(WP_{N-1|N-1})$ is *differentiable* with respect to Θ_N , enabling efficient gradient-based optimization;
- 3) Despite differentiability, the cost function is *non-convex* in the design variables, implying multiple local minima may exist;
- 4) The feasible set is convex and can be represented as a simple box constraint in polar coordinates.

We now detail how to solve the optimization problem (15) using these properties.

The first key insight is that we can take an analytical gradient with respect to the design variables, enabling efficient gradient-based algorithms. Using the identities

$$\frac{\partial(\text{tr}(X(y)))}{\partial y} = \text{tr}\left(\frac{\partial X(y)}{\partial y}\right), \quad (16)$$

and

$$\frac{\partial(X^{-1}(y))}{\partial y} = -X^{-1}(y) \frac{\partial X(y)}{\partial y} X^{-1}(y), \quad (17)$$

we obtain

$$\begin{aligned} \frac{\partial P_{N-1|N-1}}{\partial \Theta_N} &= -P_{N-1|N-1} \left[\Sigma^{-1}(\Theta_N) \bar{C}(\Theta_N) \right]^\top \begin{bmatrix} \Omega(\Theta_N) & 1 \\ 1 & 0 \end{bmatrix} \\ &\quad \times \left[\Sigma^{-1}(\Theta_N) \bar{C}(\Theta_N) \right] P_{N-1|N-1}, \end{aligned} \quad (18)$$

in which

$$\begin{aligned} \Omega(\Theta_N) &= -\left(\frac{\partial \bar{C}(\Theta_N)}{\partial \Theta_N} P_{N-1|N-1} \bar{C}^\top(\Theta_N) \right. \\ &\quad \left. + \bar{C}(\Theta_N) P_{N-1|N-1} \frac{\partial \bar{C}^\top(\Theta_N)}{\partial \Theta_N} \right), \end{aligned} \quad (19)$$

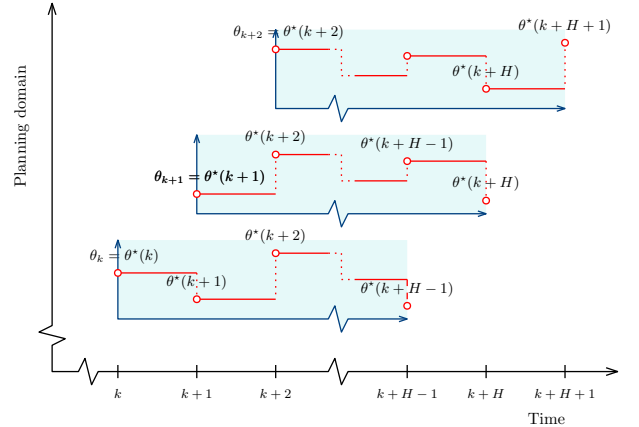


Figure 3: Schematic representation of receding horizon optimization. Starting at time k , we solve an optimization problem with a reduced horizon H to find the optimal tilts $\{\theta^*(i)\}_{i=k}^{k+H-1}$. We then store the first tilt $\theta_k = \theta^*(k)$, move up one time step in the planning domain and solve the $k+1$ -th optimization problem with the updated state $P(k+1 | k)$. We can use the previous solution $\{\theta^*(i)\}_{i=k}^{k+H-1}$ as a warm start for the next optimization problem. This process is repeated until we reach the end of the tilt sequence.

and

$$\frac{\partial \bar{C}(\Theta_N)}{\partial \Theta_N} = \begin{bmatrix} \frac{\partial C(\theta_0)}{\partial \Theta_N} A^{-(N-1)} \\ \frac{\partial C(\theta_1)}{\partial \Theta_N} A^{-(N-2)} \\ \vdots \\ \frac{\partial C(\theta_{N-1})}{\partial \Theta_N} \end{bmatrix}. \quad (20)$$

The availability of an analytical gradient is preferred over numerical approximations for efficiency and accuracy. This analytical gradient can be used within a standard constrained optimization algorithm (e.g., a projected gradient method or an interior-point method) that explicitly handles the constraints. To do so, we transform each tilt θ_k into polar coordinates (r_k, ψ_k) , where r_k is the magnitude and ψ_k is the angle. The magnitude constraints $\|\theta_k\|_2 \leq \tilde{\theta}_k$ then become simple box constraints $0 \leq r_k \leq \tilde{\theta}_k$, $0 \leq \psi_k < 2\pi$, which are readily incorporated into gradient-based solvers.

Next, since the number of design variables scales with the tilt pattern length (i.e., $2N$ scalar variables), we use receding horizon optimization (RHO) with a horizon $H < N$ to solve a sequence of reduced-size problems. At each current time k , we solve:

$$\begin{aligned} \min_{\{\theta(i)\}_{i=k}^{k+H-1}} \quad & \text{tr}(WP_{k+H-1|k+H-1}), \\ \text{s.t.} \quad & \|\theta(i)\|_2 \leq \tilde{\theta}_i, \quad i \in \{k, k+1, \dots, k+H-1\}, \\ & P_{k|k-1} \text{ given,} \end{aligned} \quad (21)$$

here, $\{\theta(i)\}_{i=k}^{k+H-1}$ denotes the design variables in the reduced-horizon tilt sequence. After solving and obtaining the optimized solution $\{\theta^*(i)\}_{i=k}^{k+H-1}$, we store the first element $\theta_k = \theta^*(k)$, calculate $P_{k+1|k}$, and repeat with $k \leftarrow k+1$ until $k = N$ (set $H = \min(H, N-k)$). This is illustrated in Figure 3. RHO, even with $H = 1$, can provide near-optimal performance [17] while reducing design variables from $2N$ to $2H$.

Since the cost function is non-convex, we employ a *multi-start strategy*, solving the RHO problem from many randomized

initial feasible sequences and selecting the best solution. Starting from $k = 1$, we introduce *warm starts* by using the best previous RHO solutions as a subset of initial sequences. We use 1000 starting points total for all optimizations, with 100 warm starts when $k \geq 1$.

Note that the solution is sensitive to system parameters $P_{0|1}$, Σ_ε , and Σ_e . While the first two can be chosen based on expert knowledge and historical data, the measurement noise covariance Σ_e can vary significantly across specimens and imaging conditions. For this reason, we propose a method to estimate it which is detailed in the next section.

3.4. Estimating sample-dependent measurement noise covariance

Different sample types and imaging conditions such as field of view and defocus affect the amount of contrast and distinguishable features within the image. Since image tracker accuracy depends on these visual characteristics, different samples and conditions typically result in different measurement noise covariances Σ_e .

To estimate the specimen-dependent Σ_e , we employ expectation maximization, alternating between Kalman smoothing (E-step) and updating the noise covariance estimate (M-step). In the M-step, we update parameters by maximizing the expected complete-data log-likelihood [18]. For the measurement noise covariance Σ_e , the update is given by

$$\Sigma_e = \frac{1}{N} \sum_{k=0}^{N-1} (y_k - C(\theta_k) \tilde{x}_{k|N-1}) (y_k - C(\theta_k) \tilde{x}_{k|N-1})^\top + C(\theta_k) P_{k|N-1} C(\theta_k)^\top, \quad (22)$$

where $\tilde{x}_{k|N-1}$ and $P_{k|N-1}$ are the smoothed state estimate and covariance, respectively, obtained from the Kalman smoother [18]. The EM algorithm is guaranteed to converge to a local maximum of the likelihood. It is advisable to run it multiple times with different initializations based on expert knowledge or rough estimates, and select the solution with the highest likelihood. This leads to the following adaptive filtering procedure.

Procedure 1. Tilt-based aberration estimation and correction with specimen-dependent tilt pattern optimization

- 1) Perform several tilt experiments with a general tilt pattern on the TEM and collect shift estimates.
- 2) Run the EM algorithm, alternating E-step and M-step (22), until convergence to estimate Σ_e .
- 3) Determine weighting matrix W , tilt pattern length N , and horizon length H , then generate an optimized tilt pattern using the method in Section 3.3.
- 4) Apply the optimized tilt pattern to the TEM and gather shift measurements.
- 5) Use the Kalman filter to estimate the aberrations.
- 6) Compensate the aberrations by adjusting the electromagnetic fields.
- 7) Repeat Steps 4-6 as necessary.

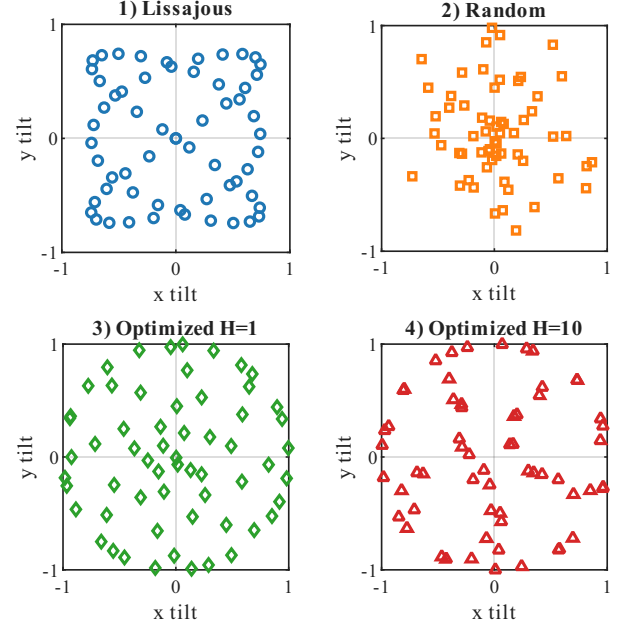


Figure 4: Comparison of different normalized tilt patterns. The patterns are: 1) Lissajous curve with frequency ratio 3:2, 2) completely randomized feasible pattern, 3) optimized pattern with $H = 1$, and 4) optimized pattern with $H = 10$.

4. Results

We present tilt pattern optimization results and experimental validation on a Thermo Fisher Scientific Krios TEM in Eindhoven, the Netherlands, following Procedure 1. A polycrystalline gold foil sample is used for optimization and validation, as it can handle high electron doses, allowing repeated application of different tilt patterns without damage.

We consider aberrations up to order $M = 4$ (14 coefficients). The sample drift is modeled using a second-order polynomial ($b = 2$) for both x and y directions, plus image rotation, bringing the total number of states to $d = 19$.

4.1. Optimized Tilt Patterns

We apply the optimization method from Section 3 to find optimal tilt patterns for TEM aberration estimation. The measurement noise covariance Σ_e for the gold foil is estimated using the EM algorithm described in the previous section. We use the interior-point algorithm to find local minimizers of (21) with tilt sequence length $N = 60$. Four tilt patterns are compared in Figure 4:

- 1) A Lissajous curve with a frequency ratio of 3:2;
- 2) A randomized pattern with a uniform distribution over the feasible set;
- 3) An optimized pattern generated using gradient-based multi-start optimization with RHO, a horizon of $H = 1$ (greedy or myopic), and a weighting matrix $W = \frac{1}{d} I_d$;
- 4) An optimized pattern generated using gradient-based multi-start optimization with RHO, a horizon of $H = 10$, and a weighting matrix $W = \frac{1}{d} I_d$.

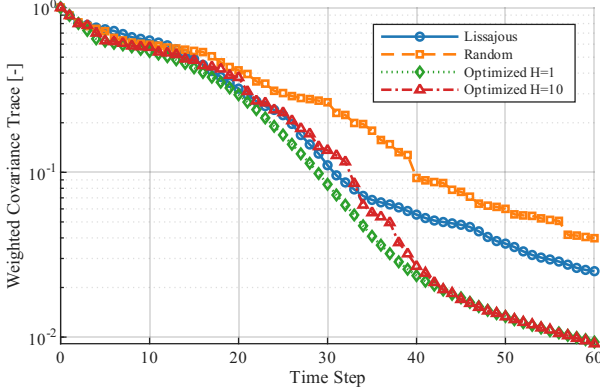


Figure 5: Weighted posterior covariance trace ($\text{tr}(WP_{kk})$) at each time index for selection of tilt patterns. In this figure, the estimation error of every normalized state x_k is weighted equally using weight matrix $W = \frac{1}{d}I_d$.

Patterns 1–2 are not optimized and are therefore expected to have poor performance in terms of the cost criterion. Pattern 3 (greedy optimization, $H = 1$) typically sacrifices some performance at the benefit of computational speed. Pattern 4 is optimized with $H = 10$ and is expected to perform well across most aberration types.

Figure 5 shows the trace of the weighted estimation error covariance WP_{kk} as a function of time index k . The 10-step optimized pattern (4) is expected to have the best performance in terms of the equally-weighted cost criterion. Interestingly, the greedy pattern (3) outperforms all other patterns at the beginning and middle of the estimation process, but falls behind pattern (4) slightly towards the end. This is expected as greedy optimization focuses on immediate gains. Note that for the greedy pattern, all intermediate patterns of lengths 1 to N are available without re-optimization, which is a practical advantage. While all patterns significantly reduce the estimates’ covariance over time, the optimized patterns typically achieve the same performance in a much shorter time span. For example, the final covariance trace of the random pattern (2) is already reached after approximately 35 time steps with the optimized pattern (3), which represents a reduction of 25 time steps or 42%.

4.2. Experimental Validation

To assess the practical performance of the estimation method and the tilt patterns, we perform over 2000 trials on an actual TEM set-up at different sample locations. At each location, we test the tilt patterns from Figure 4 in randomized order to avoid bias from time-dependent effects.

To validate aberration estimation performance, we compare each experiment’s estimated aberrations to the mean aberration estimates from experiments with similar timings and locations. This local mean can be viewed as a ground truth for the aberration values at that time and location. While this metric is sensitive to imperfect modeling, it demonstrates the variance in aberration estimates and the consistency of different tilt patterns.

We compare the experimentally realized variance in aberration estimates to the expected state estimate variance, given by the diagonal elements of $P_{N-1|N-1}$ in the KF, in Figure 6. Several

conclusions can be drawn. First, the expected state estimate variance from the KF quite closely resembles the realized variance in aberration estimates, signaling that the tilt-induced shift model is relatively accurate. Typically, realized variances are slightly higher than predicted, likely due to undermodeling of aberrations beyond $M = 4$ and non-polynomial drift. The defocus aberration (c_{20}) is notably different in this aspect, likely because defocus is retuned at different points during the experiments, violating the constant-aberration assumption. Second, optimized patterns generally outperform non-optimized patterns in terms of realized estimation variance across all aberration types. Third, the greedy pattern ($H = 1$) achieves comparable performance to the $H = 10$ pattern. In practice, the greedy pattern is preferred due to its computational efficiency and the availability of intermediate-length patterns without re-optimization.

To demonstrate the practical impact of the proposed aberration estimation method, we investigate the improvements in image quality. Figure 7 shows TEM images before and after using the alignment procedure, displaying substantially improved contrast. Compared to traditional alignment methods, the proposed method is significantly faster, reducing the full aberration correction procedure from several minutes to less than a minute.

5. Conclusion

This paper addresses the challenge of fast and accurate aberration estimation in TEM based on beam-tilt induced image shifts. We formulate the problem as a sensor scheduling task within a Kalman filtering framework, leveraging the physical relationship between electron beam tilts and image shifts to estimate multiple aberration coefficients simultaneously while accounting for their temporal drift. The tilt sequence is optimized offline using an A-optimality criterion through gradient-based receding-horizon optimization with multiple starting points to handle the non-convex cost landscape. The proposed method also allows for the prioritization of specific aberrations through a user-defined weighting matrix. We further propose an approach using EM to estimate sample-dependent model parameters.

Experimental validation on a real TEM set-up demonstrates that the optimized tilt sequences significantly outperform naive patterns, reducing the required estimation time by over 40% while achieving similar accuracy. A potential limitation is the reliance on the physical tilt-shift model. However, the experimental results indicate that the realized variance in estimates closely aligns with the KF-predicted variance, signaling that the model mismatch is limited. For this reason, the proposed methodology is deemed a promising candidate for fast and accurate TEM alignment, especially in the presence of drifting aberration parameters.

Future work could explore several promising directions. First, computational efficiency could be improved by exploiting symmetries such as rotational invariance of the tilts or constraining the search space based on observed patterns in optimized tilt sequences. Second, extending the optimization problem to include more accurate modeling of the image shift tracker could lead to the removal of the ad-hoc tilt magnitude constraints included to allow the tracker to initialize. Finally, data-driven sensor scheduling approaches could learn high-performing tilt

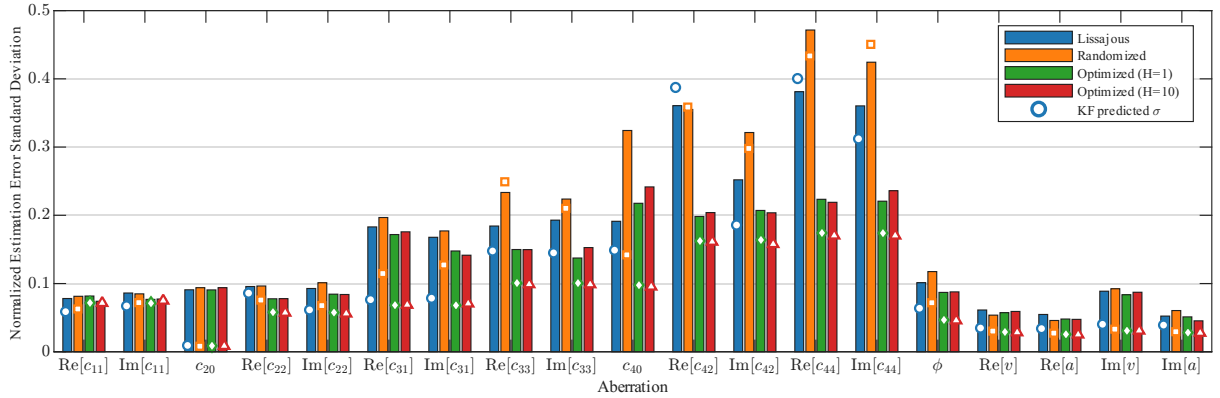


Figure 6: Comparison of the expected and realized standard deviation in aberration estimates for different tilt patterns applied to a gold sample. The markers indicate the state estimation error predicted by the Kalman filter (i.e., the square root of the diagonal elements of $P_{N-1|N-1}$), while the bars indicate the realized standard deviation in aberration estimates across many experiments. The different colors indicate different tilt patterns, which are the same as those shown in Figure 4.

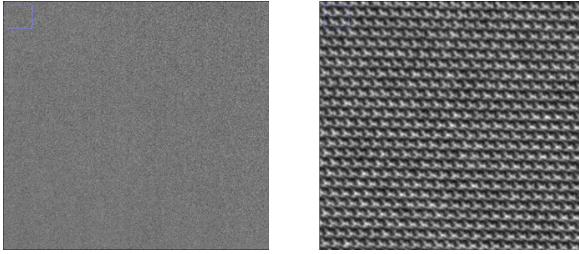


Figure 7: Illustration showing the effect of aberration correction (up to third order) on a TEM image on a SiN sample. Left: before aberration correction, in a case where the TEM is in a highly aberrated state. Right: after a few iterations of the proposed tilt-based aberration estimation and compensation method, a clear image is obtained.

policies directly from experimental data, potentially bypassing the need for exact analytical models.

References

- [1] A. C. Walls, Y.-j. Park, M. A. Tortorici, A. Wall, A. T. McGuire, D. Veesler, Structure, Function, and Antigenicity of the SARS-CoV-2 Spike Glycoprotein, *Cell* 181 (2020) 281–292.e6.
- [2] K. J. Hanszen, L. Trepte, Die Kontrastübertragung im Elektronenmikroskop bei partiell kohärenter Beleuchtung, 1971.
- [3] A. Koster, A. Van den Bos, K. van der Mast, An autofocus method for a TEM, *Ultramicroscopy* 21 (1987) 209–222.
- [4] A. Steinecker, W. Mader, Measurement of lens aberrations by means of image displacements in beam-tilt series, *Ultramicroscopy* 81 (2000) 149–161.
- [5] R. M. Glaeser, D. Typke, P. C. Tiemeijer, J. Pulokas, A. Cheng, Precise beam-tilt alignment and collimation are required to minimize the phase error associated with coma in high-resolution cryo-EM, *Journal of Structural Biology* 174 (2011) 1–10.
- [6] E. van Horssen, B. Janssen, A. Kumar, D. Antunes, W. Heemels, Image-based feedback control for drift compensation in an electron microscope, *IFAC Journal of Systems and Control* 11 (2020) 100074.
- [7] F. Zemlin, K. Weiss, P. Schiske, W. Kunath, K. H. Herrmann, Coma-free alignment of high resolution electron microscopes with the aid of optical diffractograms, *Ultramicroscopy* 3 (1978) 49–60.
- [8] F. Pukelsheim, *Optimal Design of Experiments*, Society for Industrial and Applied Mathematics, 2006.
- [9] A. C. Atkinson, A. N. Donev, R. D. Tobias, *Optimum Experimental Designs, with SAS*, May 2014, Oxford University PressOxford, 2007.
- [10] H. Zhang, R. Ayoub, S. Sundaram, Sensor selection for Kalman filtering of linear dynamical systems: Complexity, limitations and greedy algorithms, *Automatica* 78 (2017) 202–210.
- [11] K. You, L. Xie, Kalman filtering with scheduled measurements, *IEEE Transactions on Signal Processing* 61 (2013) 1520–1530.
- [12] C. Li, N. Elia, Stochastic sensor scheduling via distributed convex optimization, *Automatica* 58 (2015) 173–182. [arXiv:1403.3466](https://arxiv.org/abs/1403.3466).
- [13] Z. Sunberg, S. Chakravorty, R. S. Erwin, Information Space Receding Horizon Control for Multisensor Tasking Problems, *IEEE Transactions on Cybernetics* 46 (2016) 1325–1336.
- [14] J. Barthel, Ultra-Precise Measurement of Optical Aberrations for Sub-Ångström Transmission Electron Microscopy, Phd thesis, Technischen Hochschule Aachen, 2003.
- [15] D. Bolme, J. R. Beveridge, B. A. Draper, Y. M. Lui, Visual object tracking using adaptive correlation filters, in: 2010 IEEE Computer Society Conference on Computer Vision and Pattern Recognition, IEEE, 2010, pp. 2544–2550.
- [16] R. E. Kalman, A New Approach to Linear Filtering and Prediction Problems, *Journal of Basic Engineering* 82 (1960) 35–45.
- [17] D. Mayne, J. Rawlings, C. Rao, P. Scokaert, Constrained model predictive control: Stability and optimality, *Automatica* 36 (2000) 789–814.
- [18] S. Gibson, B. Ninness, Robust maximum-likelihood estimation of multivariable dynamic systems, *Automatica* 41 (2005) 1667–1682.